Investigating the Influences of Crustal Thickness and Temperature on the Uplift of Mantle Material Beneath Large Impact Craters on the Moon

Min Ding[1], Jason M. Soderblom[2], Carver J. Bierson[3], Maria T. Zuber[2]

[1]State Key Laboratory of Lunar and Planetary Sciences, Macau University of Science and Technology, Taipa, Macau.

[2]Department of Earth, Atmospheric and Planetary Sciences, Massachusetts Institute of Technology, Cambridge, MA 02139, USA.

[3]Department of Earth and Planetary Sciences, University of California Santa Cruz, Santa Cruz, CA 95064.

Corresponding author: Min Ding (miding@must.edu.mo)

Key Points:

- The minimum crater diameter for which impacts result in mantle uplift depends on local crustal thickness.
- The magnitude of mantle uplift is primarily controlled by impact energy and thus is correlated with impact diameter.
- Statistical indistinguishability between the SPA and FHT craters provides an upper limit on the thermal difference.

Abstract

In this work, we examine variations in mantle uplift associated with large lunar impact craters and basins between major terranes. We analyze the Bouguer gravity anomalies of 100–650-km diameter lunar impact craters using Gravity Recovery and Interior Laboratory (GRAIL) observations and the Lunar Orbiter Laser Altimeter (LOLA) crater database. The Bouguer gravity anomalies of 324 large impact craters analyzed herein are primarily controlled by the uplifted crust-mantle (Moho) interface in the central region of these impact craters, although post-impact mare deposits contribute to the gravity anomalies of some individual craters. The central uplift of the Moho interface is primarily controlled by impact energy and increases to ~ 30 km for a 650-km crater. Further analyses of craters in the Feldspathic Highlands Terrane (FHT) with varied crustal thickness (T_c) reveal that the onset crater diameter (D_{min}) with an uplifted Moho interface is dependent on the local T_c: $D_{min} \sim 146+1.1T_c$ (in a unit of km). This equation also provides a quantification of the depth-dependent attenuation of impact-induced structural uplift, using the Moho uplift as a proxy for structural uplift. Moho uplift of large craters in the hotter South Pole-Aitken Terrane (SPA) is not statistically different from FHT craters, consistent with the expected thermal difference between these terrains during the pre-Nectarian period.

Plain Language Summary

Gravitational signatures of large impact craters and basins reveal notable mantle uplifts under the crater floor. The underlying mantle uplift is significant for lunar basins with a crater diameter larger than ~ 200 km and is one of the main characteristics of peak-ring and multi-ring basins. The magnitude of mantle uplift linearly increases with crater diameter, which itself relates to an increase in impact energy. It has been suggested that the target properties, including the crustal thickness and thermal state, affect the crater mantle uplift as well. In this study, we investigate the relationship between target properties and the crater gravitational signature by statistical analysis. The analysis provides a quantification for the effect of the crustal thickness on the onset of mantle uplift and a constraint on the thermal difference between highland and South Pole-Aitken basin terranes.

1 Introduction

It has long been recognized that both terrestrial and lunar impact basins are associated with notable uplifts of mantle materials (Pilkington & Grieve, 1992; Cintala & Grieve, 1998). This impact-induced mantle uplift has been investigated by both laboratory (e.g., Schmidt & Housen, 1987) and numerical experiments (Potter et al., 2013; Milbury et al., 2015). On the Moon, the onset of the mantle (or more precisely the crust-mantle boundary, Moho) uplift coincides with the morphologic transition from complex craters to peak-ring basins. This coincidence has strong implications for the formation mechanism of the peak ring, which has been suggested to be controlled by the interaction between the inward collapse of crustal blocks and the underlying central uplift (Potter, 2015; Baker et al., 2016). Crater dynamic considerations imply that in addition to the impact conditions (e.g., impact energy and impactor density), target properties also influence the Moho uplift. Quantifying the effects of target parameters is thus of fundamental interest for fully understanding the impact cratering process.

High resolution and precision gravity data from the Gravity Recovery and Interior Laboratory (GRAIL) mission (Zuber et al., 2013) provide an unprecedented opportunity to investigate the

internal structure of impact craters and to infer crater formation and modification processes. Unlike surface topography, which degrades over time, leading to the loss of evidence of ancient impact basins, the underlying Moho interface is better preserved and can be inferred from gravity data. GRAIL gravity data, for example, have been used to identify previously unknown impact basins (Neumann et al., 2015). GRAIL gravity also provides constraints on the diameter onset of the central Moho uplift. A global onset crater diameter of ~ 200 km has been found (Soderblom et al., 2015; Baker et al., 2017). However, there has yet to be a systematic study to investigate the effect of target properties on the Moho uplift of the impact craters.

In this study, we use the Bouguer gravity anomalies of 100–650-km diameter impact craters to infer the central uplifts of the underlying Moho interface, after considering the effects of post-impact mare infills. We then analyze the effects of crater diameter and crustal thickness on the Moho uplift using craters in the Feldspathic Highlands Terrane (FHT). By comparing the FHT craters with the craters in the South Pole-Aitken Terrane (SPA), we infer the effects of thermal state difference. Because we consider a wide range of impact morphologies, from complex craters to proto-basins, and from peak-ring basins to multi-ring basins (e.g., Baker et al., 2012, 2016, 2017), for simplicity we refer to them all as impact craters.

2 Data and Parameters

2.1 Central Bouguer gravity anomaly

We analyze 324 impact craters with rim diameters (D_c) of 100–650 km identified in the Lunar Orbiter Laser Altimeter (LOLA) crater database (Head et al., 2010; Kadish et al., 2011; Figure 1). We use the GRAIL free-air gravity anomaly model JGGRAIL_1200C12A (Konopliv et al., 2014), and then derive the Bouguer gravity model by subtracting the gravitational contribution of topography. Our Bouguer correction assumes the laterally varying crustal density model from Wieczorek et al. (2013), with the unconstrained density of the mare region interpolated from existing data points. Spherical harmonic degrees > 600 are excluded due to their low signal-to-noise ratio. In the sensitivity test (3.3), we test the application of a high-pass filter $l_{min} = \frac{\pi R_0}{D_c}\ and\ \frac{2\pi R_0}{D_c}$ (corresponding to a block-size resolution of the crater diameter and radius, respectively) to each crater in order to remove gravity signals that are significantly larger than, and therefore irrelevant to the crater, similar to Bierson et al. (2016). Here R_0 is the reference radius of the Moon and is set to 1738 km. Local Bouguer gravity model for each crater is then referenced to 60 km (i.e., maximum local crustal thickness) above the local topography. The topography model is the most recent from the Lunar Orbiter Laser Altimeter (LOLA) (Smith et al., 2016).

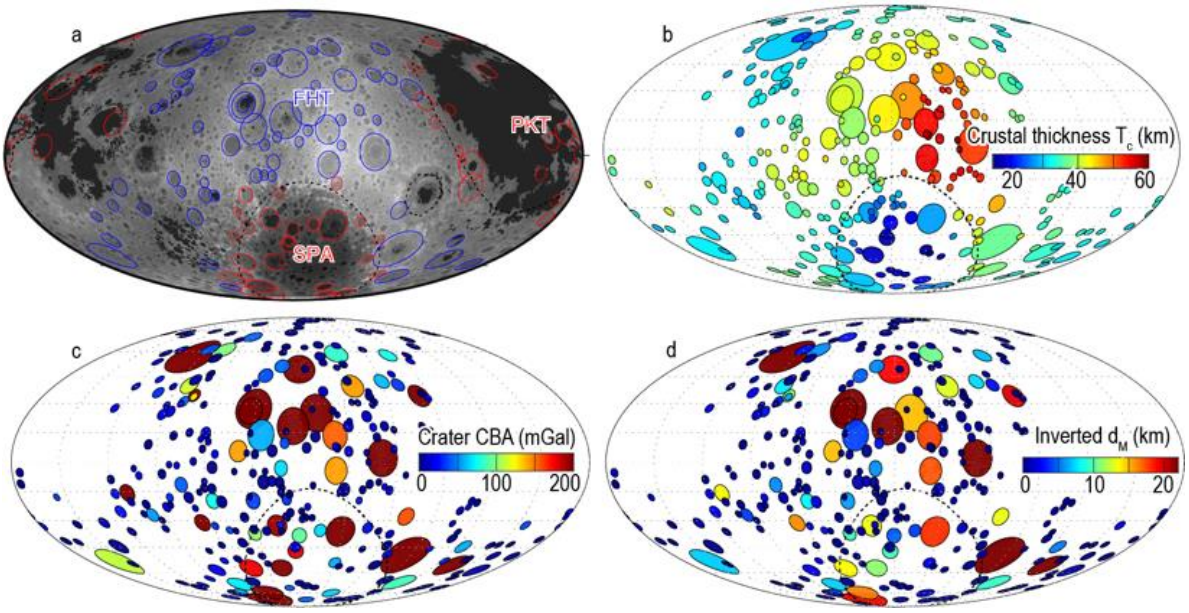

Figure 1. (a) Craters considered in this study located in the FHT, SPA, and Procellarum KREEP Terrane (PKT) projected on a gray-scale LOLA topography map in a Mollweide pseudo-cylindrical projection centered on the farside. Dashed curves outline the three major crustal terranes. Dark gray patches are mare basalts. (b) Crustal thickness averaged in each crater area based on the first crustal thickness model of Wieczorek et al. (2013). (c) Measured central Bouguer anomalies (CBA) of craters. (d) Inverted Moho uplift (d_M) in the crater central region.

For each crater, the Bouguer gravity signature is characterized by a single measurement, the central Bouguer anomaly (CBA). Following Soderblom et al. (2015), CBA is defined as the difference between the area-weighted average Bouguer anomaly of the central region with a radial distance less than 0.2*R* (*R* is the crater radius) and that of the annular region from 0.5 to 1*R*. To assist the data analysis, we estimate the uncertainty of the crater CBA values as the standard deviation of the Bouguer gravity data points (with a block size of 9 km) within the central circular region. The corresponding *p*-value measures the probability for a two-sample t-test statistic to be more extreme than the observation under the null hypothesis that the mean Bouguer anomaly within the central circular region is less than or equal to that in the reference annulus. Small *p*-value casts doubt on the validity of the null hypothesis and therefore implies the CBA is indeed larger than zero. These crater parameters, as well as the other parameters in the following sections, are included in the crater parameter database (Table S1).

2.2 Mare infills and central Moho uplifts

The crater CBA is influenced by both post-impact mare infilling and mantle uplift. Other internal structures that influence gravity data, from the impact-induced melt (Cintala & Grieve, 1998) and porosity change (Milbury et al., 2015), to post-impact breccia infills, all extend to the crater rim. This spatial scale is too large to contribute to crater CBA in the central region within 0.2*R*. After quantifying and subtracting the gravitational effect of post-impact mare infills, we invert for the relief of the crust-mantle (Moho) interface.

Quantification of post-impact mare infills requires a spatial distribution map of mare basalts (Nelson et al., 2014). For a typical farside mare crater, Poincaré basin (Figure 2), we estimate the

mare coverage within the central region (inside 0.2*R*) to be 85% and mare coverage within the surrounding annular region (with a radial distance of 0.5*R* to *R*) to be 27%. The thickness of the mare basalts is uncertain, but the maximum thickness can be determined by the difference between the observed and modeled fresh-crater depth (using scaling relationship from Pike, 1977; Kalynn et al., 2013; see details in Ding et al., 2018). Assuming a mare density of 3,150 kg/m^3 and varied local crustal density (2,690 kg/m^3 for Poincaré basin), we calculate the gravitational attraction due to mare infills in the spherical domain using the opensource software SHTools (Wieczorek & Phillips, 1998; Wieczorek & Meschede, 2018). The corresponding maximum estimate for the CBA value due to mare infills is 49 mGal. This calculation has been conducted for all the craters, yielding maximum CBA estimates due to mare infilling (Table S1).

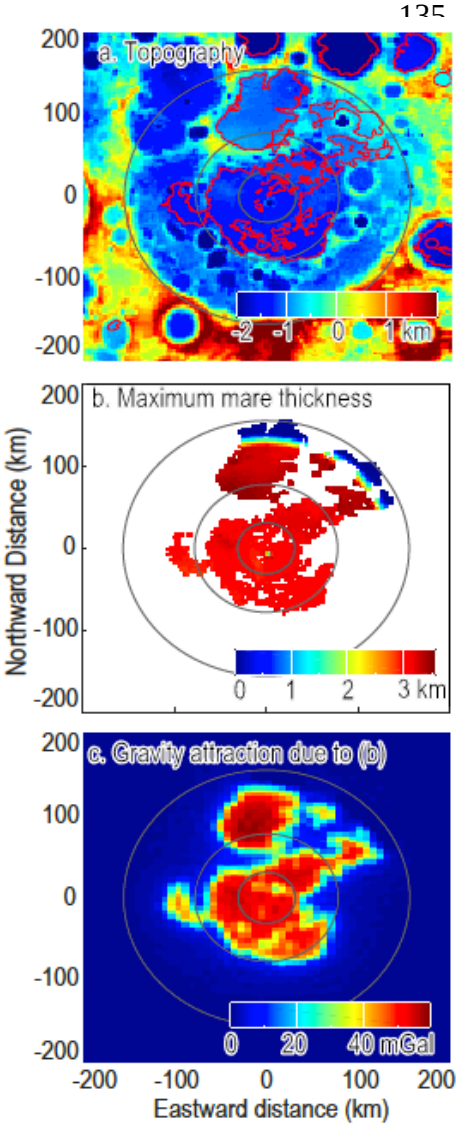

Figure 2. (a) Topography and mare basalt distribution (red contours) for Poincaré basin; (b) Estimated maximum thickness of potential mare infills; (c) Modeled gravity attraction due to (b). The dark-gray circle indicates the central region (<0.2*R*) for CBA calculation. The surrounding annular region extends from 0.5 to 1*R* and is indicated by light-gray circles

Next, we invert the Bouguer anomaly for the Moho relief, and derive the amount the Moho is uplifted (d_M) within each crater. The inversion for the Moho relief is conducted using SHTools and the variable crustal density model from Wieczorek et al. (2013) again. But in this inversion, we update the gravity model with higher precision and resolution, which permits a higher $\lambda_{1/2}$

value of 120 (in comparison with 80 in Wieczorek et al., 2013) for the high-frequency filter. This high-frequency filter, which is required for the inversion algorithm to converge, is characterized by $\lambda_{1/2}$, the spherical harmonic degree at which the high-frequency filter reaches a value of 0.5. We find, however, that our results (Section 3) are insensitive to the correction for post-impact mare basalts or the $\lambda_{1/2}$ value.

The Moho uplift d_M is measured as the difference between the area-weighted Moho relief in the central region with a radial distance < 0.2R and that of the reference annular region from 0.5 to 1R, spatially similar to the definition of the crater CBA (Soderblom et al., 2015). d_M values are provided in Table S1.

2.3 Candidate control parameters

The candidate control parameters for d_M include the impact energy and target properties, most notably crustal thickness and target temperature (Figure 3). The impact energy (affected by a combination of impact velocity, size and angle) cannot be directly measured, but is correlated with D_c. At the same time, d_M is observed to correlate with D_c (e.g., Soderblom et al., 2015; Baker et al., 2017), suggesting that impact energy is a primary control of d_M.

The influences of target properties on d_M are more nuanced and require additional analysis to constrain. Impact hydrocode simulations suggest that decreasing crustal thickness (T_c) enhances the Moho uplift (Milbury et al., 2015), whereas the effect of crustal porosity on the Moho uplift is limited. The thermal effects are multifold. A hotter target yields lower material strength and viscosity with enhanced impact melting, and thus is expected to result in larger Moho uplift (Potter et al., 2013). Simultaneously, more significant post-impact viscoelastic relaxation in a hotter target tends to reduce the Moho uplift (Kamata et al., 2015). The net outcome of these two mechanisms requires further quantification, but may result in little to no appreciable change in the Moho uplift. An additional complication in interpreting our results is that a hotter thermal state results in a larger crater for a given impact energy (Miljković et al., 2013, 2016), and therefore indirectly influences the relationship between d_M and D_c.

We analyze the GRAIL data to constrain the influences of each of these target properties. We derive T_c from the first model of Wieczorek et al. (2013), obtaining values that range from 15 to 65 km (Table S1). To consider different thermal states, we compare FHT and SPA (Section 3.2). While PKT almost certainly has yet another thermal state, the paucity of PKT craters (Figure 1) makes it impossible to conduct statistical analysis for this region. Crater ages from Losiak et al. (2009) are also included in Table S1. Although crater age is expected to correlate with the target temperature (at the time of crater formation) and thus the Moho uplift, the dominance of a single pre-Nectarian age prohibits the quantification of crater age effects.

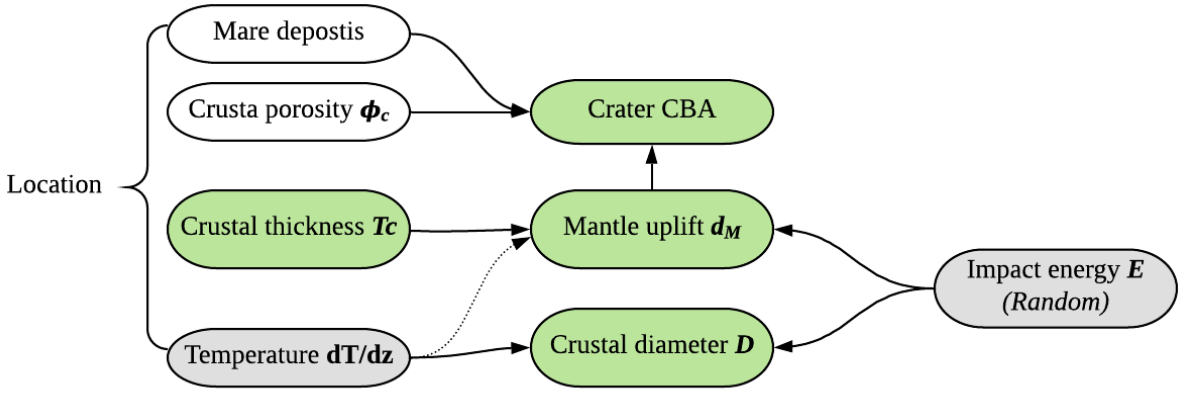

Figure 3. Flow chart showing candidate control parameters on the crater CBA and central Moho uplift. Green colors indicate availability of direct observations, while gray colors indicate parameters that can only be inferred.

3 Results and Discussions

3.1 FHT: Effect of crustal thickness and implications

To examine the effects of crustal thickness on Moho uplift, we consider 232 craters in the FHT. We fit these data to a two-slope model that assumes the CBA values are equal to zero for a crater diameter (D_c) less than the onset diameter D_{min}, but linearly increase when $D_c > D_{min}$ (Figure 4a). We estimate D_{min} to be 213±34 km. The best-fit value and uncertainty are given by the mean and standard deviation of 1,000 resampled datasets using a bootstrap re-sampling method. Our best-fit value is similar with Soderblom et al. (2015), but the uncertainty is larger because we consider a smaller number of craters. For the linearly increasing portion of the two-slope model, we find a slope of 0.86±0.17 mGal/km. Because of the linear relationship assumed for $D_c > D_{min}$ craters, the best-fit D_{min} is sensitive to the CBA values of impact craters much greater than 200 km.

The onset of CBA > 0 is better quantified by a limited portion of craters with CBA values close to zero. For statistical robustness, we use the *p*-values of the crater CBAs to divide the craters into two groups: positive CBA group (*p*-value less than 0.05; red dots in Figure 4b) and negative CBA group (other craters; gray dots). We apply a linear discriminant analysis to find a linear decision boundary between the two groups, using T_c and D_c as control parameters. The coefficients of the decision boundary $D_{min} = cT_c + d$ are estimated to be c = 1.1±1.2 and d = 146±46 km, with uncertainties estimated by bootstrap re-sampling. The D_{min} value estimated by the linear discriminant analysis is smaller than that in the two-slope model, though the results agree within error. The positive best-fit value for c, the parameter describing the dependence on T_c, is consistent with physical considerations and numerical simulations (Milbury et al., 2015) that predict that it is harder for impacts to induce Moho uplift in a thicker crust than in a thinner crust, though this is only a 1-sigma detection and should be considered with appropriate caution. As CBA mainly represents the central Moho uplift, this decision boundary quantifies the effect of crustal thickness on the onset of central Moho uplift.

For the craters with CBA > 0, we analyze the magnitude of the uplift d_M. The usage of $D_c - cT_c - d$ as the predictor parameter ensures that the central Moho uplift d_M starts from zero, and that the effects of T_c and D_c are consistently included. We find a regression coefficient, e, of 0.068±0.005. This model is robust as it is insensitive to the reference radius of the gravity model, post-impact mare correction, and high-frequency filter in the gravity inversion (see Section 3.3). The outliers in Figure 4c are discussed in Section 3.3. It is worth noting that a direct two-variable linear regression for D_c and T_c yields a positive regression coefficient for T_c that is inconsistent with physical considerations and the previous linear discriminant analysis. However, a high p-value for T_c suggests that the effect of T_c is insignificant (verified by correlation analysis and feature selection, e.g., relaxed lasso regression). This indicates that it is impossible to quantify the contribution of T_c variations to the Moho uplift using these data and a two-variable linear regression. This is likely due to the combined effects of large scatter in the data and limited data for large craters.

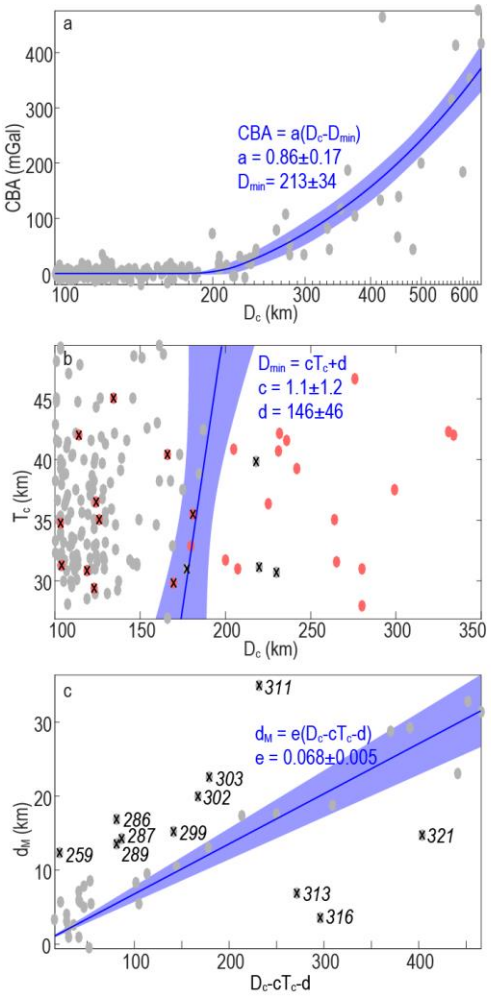

Figure 4. (a) Two-slope model (blue curve and shaded region) for the CBA values (gray dots) of the FHT craters. (b) Linear classification of the FHT craters: red dots are positive CBA group (p-value < 0.05); gray dots are negative CBA group. Blue line is the estimated decision boundary with shaded uncertainty region. Cross marks indicate misclassified points. (c) Linear regression for the FHT craters with positive CBAs plotted in (b). Notable outliers (different from those in b) are marked by their crater ID numbers in Table S1. Model and parameter uncertainties are standard deviations (i.e., 68% confidence intervals).

Using T_c as a proxy for the varied crustal layer depth (z) beneath one single crater, the Moho uplift d_M represents the depth-dependent structural uplift due to this impact event (Figure 5). For a given impact diameter D_c, the minimum layer depth z_0 with zero structural uplift is determined by the decision boundary $D_c = cz_0 + d$. By further assuming that the structural uplift follows the

observation-based linear relationship $d_M = e(D_c - cz - d)$ (Figure 5c), we calculate a second critical depth z_1 when the uplifted crustal or mantle material in the crater central region reaches the surface. The exposure of deep materials may provide insights into the lunar composition and stratification, although the central-peak and peak-ring materials are most commonly used (Cintala & Grieve, 1998; Tompkins & Pieters, 1999; Kring, 2009). The numerical models of Potter et al. (2013) overestimate z_0 and z_1 by a factor of ~2 and the structural uplift (d_M) by a factor of ~ 4 (Figure 5b–c), likely due to lower strength parameters used in their hydrocode models.

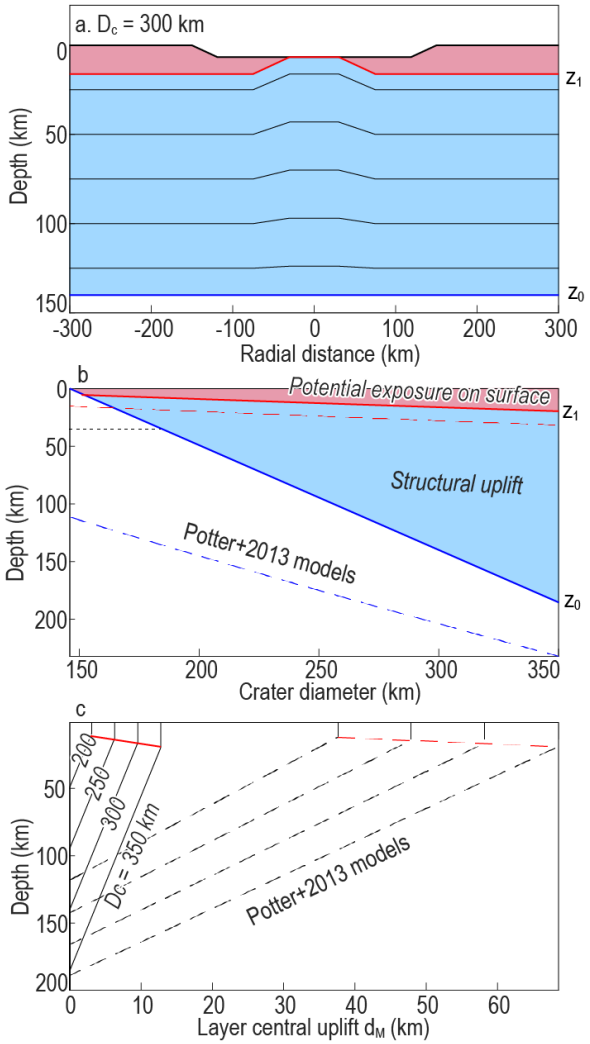

Figure 5. (a) Predicted structural uplifts at varied layer depths (z) for a typical 300-km diameter crater. (b) Two regimes of structural uplift controlled by the layer depth and crater diameter. (c) Predicted structural uplift at a depth z for 200–350 km diameter craters. Dashed lines are models from Potter et al. (2013).

3.2 SPA: Effect of temperature and implications

We apply the same statistical analysis to the 51 SPA craters we examined. Figure 6 shows no statistical difference between the SPA and FHT craters, although the crater CBA for D_c less than 213 km is -4.6±1.7 mGal. This slightly negative CBA is likely due to lower porosity in the SPA (Milbury et al., 2015; Ding et al., 2018). The similar size-dependent behavior of SPA and FHT crater CBAs indicates that the SPA thermal state effects are limited on Moho uplift.

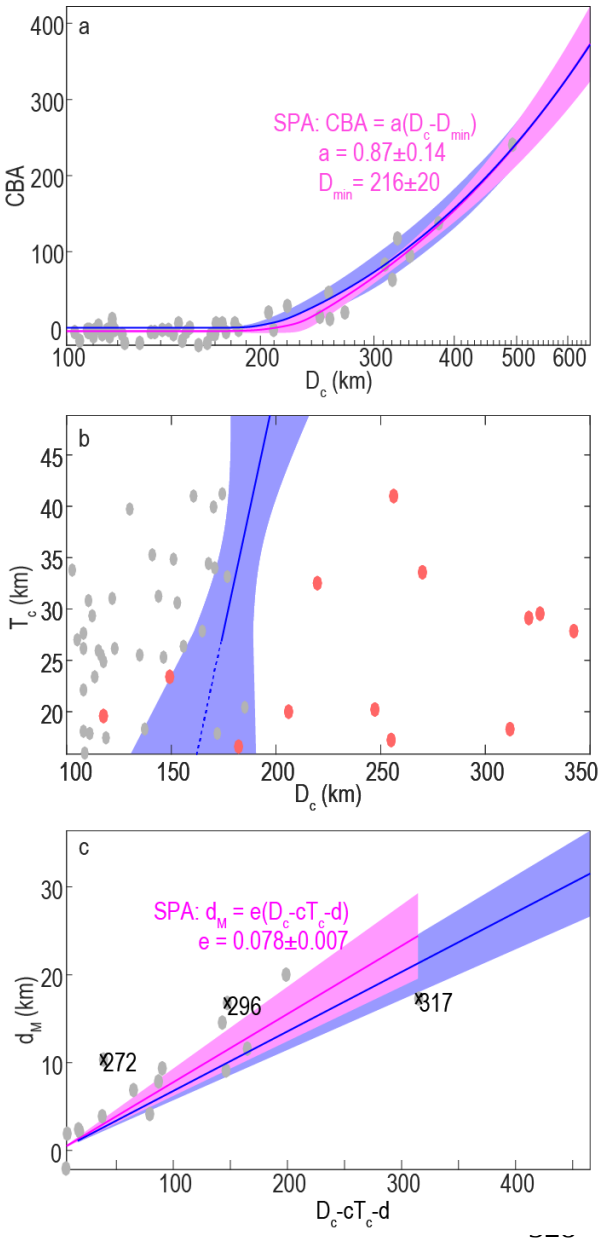

Figure 6. Similar to Figure 4 but for SPA craters (dots). (a) Two-slope model and (c) linear model for SPA craters are shown in magenta color, which matches well with the results for FHT craters (blue color). Besides, (b) the decision boundary for FHT craters (blue) also well separate SPA craters.

To further interpret this result, we consider the thermal history of the SPA region. Comparing with FHT, this region's thermal state is influenced by two factors: impact heating from the SPA impact and lack of radiogenic heating due to impact excavation of crustal materials (Figure 7a). SPA impact heating has been modeled to last ~100 Ma after the initial impact (Rolf et al., 2017). The decrease in radiogenic heating can be estimated by the time-dependent radiogenic heating of uranium (U), thorium (Th) and potassium (K), assuming a Th concentration of 1 ppm, a Th/U ratio of 3.7 and a K/Th ratio of 460 for the lunar crust (Laneuville et al., 2018). Heat generation rates and half-lives of the radiogenic elements are from Turcotte & Schubert (2014). The radiogenic heat rate is then multiplied by the excavated thickness of crustal materials (T_{exc}) in SPA to yield the surface heat flux. We consider T_{exc} ranging from 10 to 35 km; the lower limit is from gravity analysis (Wieczorek et al., 2013; Taylor & Wieczorek, 2014), while the upper limit

is derived from hydrocode simulations (Potter et al., 2012; Zhu et al., 2019). Combining the effects of impact heating and lack of radiogenic heating, we find that the surface heat flux in SPA was greater than that in the FHT for the first ~90 Ma after the SPA formation, but less than FHT afterwards (Figure 7a). The reference FHT thermal evolution path is from Laneuville et al. (2013).

To relate these thermal states to target properties for individual impact craters requires knowing the timing of each impact. Because the precise dating of impact craters is not available, we use the standard cumulative crater density function (Neukum et al. 2001; Figure 7b) to normalize the surface heat flux, yielding the average heat fluxes sampled by the SPA and FHT craters in the entire pre-Nectarian period (Figure 7c). We consider the pre-Nectarian period from the SPA formation age to 3.9 Ga. Although the age of SPA basin is found to be 4.25–4.3 Ga from isotopic dating and crater counting (Orgel et al., 2018; Garrick-Bethell et al., 2020), the age is uncertain due to the debatable source of the dated samples and uncertainty in the early cratering chronology. So here we test a range of 4.1–4.45 Ga for the SPA formation age.

We consider the temperature-induced D_c variability to quantify the thermal effect, assuming the other two thermal mechanisms (Section 2.3) yield no appreciable net effect. Impact hydrocode modeling by Miljković et al. (2016) suggests that while D_c is sensitive to the thermal state, the transient crater diameter D_t depends only on the impact energy. The scaling relationship $D_t = fD_c^g$ is thus useful for estimating D_c in varied target thermal state. Miljković et al. (2016) find $f_1 = 2.92$ and $g_1 = 0.77$ for the nearside with a surface temperature gradient of 20 K/km (corresponding to a surface heat flux of 60 mW/m^2 assuming a crustal heat conductivity of 3 W/m/K), and $f_2 = 2.48$ and $g_2 = 0.84$ for the FHT with a surface temperature gradient of 10 K/km (corresponding to 30 mW/m^2). Assuming that the coefficients f and g are linearly related to the surface heat flux, we can estimate the change of D_c with surface heat flux. Figure 7d shows the expected average crater diameter for an impact into SPA as a function of SPA formation age for a nominal impact event that would form a 300-km FHT crater (assuming the average heat flux in Figure 7c). CBA values for the FHT and SPA craters are statistically insignificant, requiring Dc^* to lie within an uncertainty range of ~35 km. The overlap in thermal models (Figure 7d) is consistent with the similarity in the observed CBA values. No additional constraints on T_{exc} and the SPA formation age is obtained, although larger T_{exc} and earlier SPA formation age are preferred.

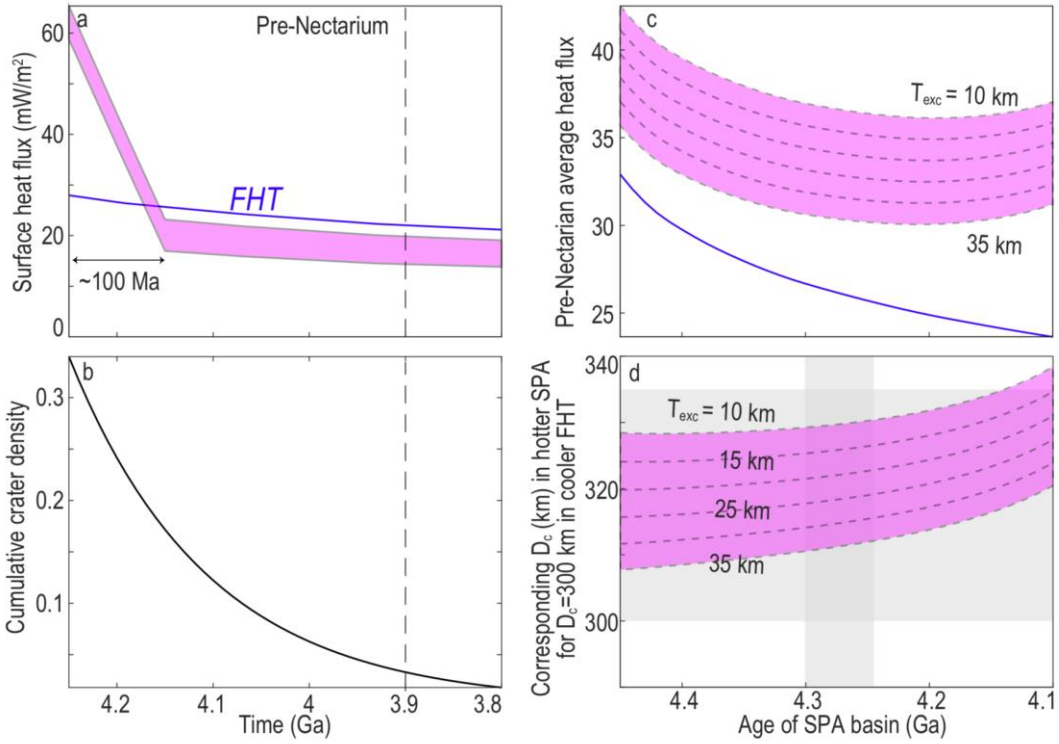

Figure 7. (a) Modeled SPA thermal evolution (magenta) that includes the increased heat from the SPA impact and the loss in radiogenic heating of a 10–35 km crust from the FHT thermal evolution path (blue), assuming a SPA formation age of 4.25 Ga. (b) Cumulative crater density (with a crater diameter larger than 1 km per area of 1 km^2) from Neukum et al. (2001). (c) Average surface heat flux sampled by impact craters in the pre-Nectarian period as a function of the formation age of SPA, ranging from 4.1 to 4.45 Ga. (d) The expected crater diameter D_c^* for an impact with the same energy that would form a 300-km FHT crater, in the hotter SPA region, plotted against the SPA formation age. The overlap between the gray and magenta regions suggest that the observed statistical similarity is consistent with the modeled thermal difference.

3.3 Model sensitivity and other influential factors

Although individual CBA and d_M values are dependent on the details of the gravity modeling and inversion, our statistical results are robust. Table 1 shows the sensitivity of the estimated coefficients to key steps of the derivation of the crater CBA and d_M data. While the correction for post-impact infills and the change of $\lambda_{1/2}$ value in the gravity inversion does not show a noticeable effect, the use of the laterally varying crustal density model from Wieczorek et al. (2013) is critical: if a uniform crustal density of 2,550 kg/m^3 is used instead of the variable crustal density model, D_{min} and d would become systematically smaller. In addition, SPA would seemingly be associated with smaller D_{min} because of regional higher crustal density. Application of local high-pass filter to each crater strengths the crater-scale variability, particularly in the SPA region. But those crater-scale variability is related to not only deep Moho uplift, but also near-surface materials (e.g., mare). The results with the larger $l_{min} = \frac{2\pi R_0}{D_c}$ is greatly influenced

by near-surface materials: SPA craters show much lower D_{min}, likely due to more extensive surface mare distribution.

Table 1. Model sensitivity to parameters

Model Settings		*a, mGal/km*	*D_{min}, km*	*c*	*d, km*	*e, 10^{-2}*
Reference (Section 3.1)	FHT	0.86±0.17	213±34	1.1±1.2	146±46	6.8±0.5
	SPA	0.87±0.14	217±20	3.3±1.6	115±46	8.0±0.6
Uniform crust density	FHT	0.97±0.13	166±13	1.0±2.1	124±78	6.9±0.5
	SPA	1.23±0.17	156±15	3.9±1.7	96±47	8.6±1.1
High-pass filter $l_{min}=\frac{\pi R_0}{D_c}$	FHT	0.88±0.18	208±33	N/A		
	SPA	0.80±0.13	200±20			
High-pass filter $l_{min}=\frac{2\pi R_0}{D_c}$	FHT	0.75±0.16	217±35			
	SPA	0.53±0.11	178±20			
Mare infills corrected	FHT	0.85±0.18	216±34	1.1±1.2	144±45	6.8±0.5
	SPA	0.92±0.33	229±28	3.3±1.6	116±46	7.8±0.7
$\lambda_{1/2}$=80	FHT	N/A				6.9±0.5
	SPA					8.1±0.5

The outliers in Figures 4c and 6c are craters with gravity signatures that are not well explained by Moho uplift. By looking at individual craters, we find that most of the high-CBA outliers are explainable by the existence of mare, cryptomare, or co-existence of two impact craters (i.e., double impact). Among them, the Szilard North crater (with a crater ID number of 259) overlaps with a smaller Szilard crater (132), and the Moscoviense crater (311) overlaps with Moscoviense North (323). The TOPO-13 (272), Schrödinger (296), Lorentz (302), and Schiller-Zucchius (303) craters are associated with mare basalts that are likely thicker than in other craters. The rest, Milne (286) and Balmer-Kapteyn (287) (as well as TOPO-13 and Schiller-Zucchius) craters, are associated with high-density cryptomare materials (Whitten & Head, 2015), contributing to the large CBA. Our interpretation that mare infilling explains much of the observed variability in the CBA values is supported by the fact that we observe far fewer low-CBA outliers in the data. The extremely low-CBA craters, including the Mutus-Vlacq (313) and Kohlschutter-Leonov (316) craters, are probably not impact craters but rather topographic depressions surrounded by thick impact ejecta (Byrne, 2016).

In addition to crater diameter, crustal thickness and thermal state, impact characteristics including impact energy (size, velocity and impact angle) and impactor composition also influence the crater CBA and Moho uplift. Shorter-wavelength variability in the target material properties, thermal state and crustal thickness not included in our analysis may contribute to the CBA variability, too. The effects of crater age and non-homogenous thermal evolution of the Moho uplift requires more comprehensive numerical simulations and more precise dating of impact craters.

4 Conclusions

By linking the gravity signatures of large impact craters to the lunar crustal thickness and a lunar thermal evolution model, we investigate the effect of crustal thickness and thermal state on the onset and magnitude of impact-induced Moho uplift.

The onset of the Moho uplift is primarily controlled by the crater diameter, and is likely negatively influenced by crustal thickness. The dependence on the crustal thickness implies structural uplift attenuation with depth. The gravity observations reveal less structural uplift than numerical results of Potter et al. (2013), likely due to lower strength parameters used in the hydrocode models.

The statistical similarity between the FHT and SPA craters suggests that the thermal difference of the two terranes is not significant enough to introduce a noticeable difference in Moho uplift. Existing impact simulation results are consistent with the SPA thermal models.

Extremely high CBA observations exist for mare craters, double craters, and craters with cryptomare, while extremely low CBA observations imply topographic lows not associated with impact craters.

Acknowledgments, Samples, and Data

Gravity and topography models used in this study are retrieved from the Geophysics Node of the Planetary Data System. Derived crater parameters are provided in Tables S1 and available in a zenodo repository (http://doi.org/10.5281/zenodo.3833814). We are grateful to Mark Wieczorek for providing the opensource software SHTools and consultation. We thank Francis Nimmo and Ye Luo for invaluable discussions. This work is supported by CAS XDB41000000, NSFC 41806067, and CNSA D020303.

References

Baker, D. M. H., Head, J. W., Neumann, G. A., Smith, D. E., & Zuber, M. T. (2012). The transition from complex craters to multi-ring basins on the Moon: Quantitative geometric properties from Lunar Reconnaissance Orbiter Lunar Orbiter Laser Altimeter (LOLA) data: GEOMETRIC PROPERTIES OF BASINS FROM LOLA. *Journal of Geophysical Research: Planets*, *117*(E12), n/a-n/a. https://doi.org/10.1029/2011JE004021

Baker, D. M. H., Head, J. W., Collins, G. S., & Potter, R. W. K. (2016). The formation of peak-ring basins: Working hypotheses and path forward in using observations to constrain models of impact-basin formation. *Icarus*, *273*, 146–163. https://doi.org/10.1016/j.icarus.2015.11.033

Baker, D. M. H., Head, J. W., Phillips, R. J., Neumann, G. A., Bierson, C. J., Smith, D. E., & Zuber, M. T. (2017). GRAIL gravity observations of the transition from complex crater to peak-ring basin on the Moon: Implications for crustal structure and impact basin formation. *Icarus*, *292*, 54–73. https://doi.org/10.1016/j.icarus.2017.03.024

Bierson, C. J., Phillips, R. J., Nimmo, F., Besserer, J., Milbury, C., Keane, J. T., et al. (2016). Interactions between complex craters and the lunar crust: Analysis using GRAIL data. *Journal of Geophysical Research: Planets*, *121*(8). https://doi.org/10.1002/2016JE005090

Byrne, C. J. (2016). *The Moon's Largest Craters and Basins*. Cham: Springer International Publishing. https://doi.org/10.1007/978-3-319-22032-1

Cintala, M. J., & Grieve, R. A. F. (1998). Scaling impact melting and crater dimensions: Implications for the lunar cratering record. *Meteoritics & Planetary Science*, *33*(4), 889–912. https://doi.org/10.1111/j.1945-5100.1998.tb01695.x

Ding, M., Soderblom, J. M., Bierson, C. J., Nimmo, F., Milbury, C., & Zuber, M. T. (2018). Constraints on Lunar Crustal Porosity From the Gravitational Signature of Impact Craters. *Journal of Geophysical Research: Planets*, *123*(9), 2281–2294. https://doi.org/10.1029/2018JE005654

Garrick-Bethell, I., Miljković, K., Hiesinger, H., van der Bogert, C. H., Laneuville, M., Shuster, D. L., & Korycansky, D. G. (2020). Troctolite 76535: A sample of the Moon's South Pole-Aitken basin? *Icarus*, *338*, 113430. https://doi.org/10.1016/j.icarus.2019.113430

Head, J. W., Fassett, C. I., Kadish, S. J., Smith, D. E., Zuber, M. T., Neumann, G. A., & Mazarico, E. (2010). Global distribution of large lunar craters: Implications for resurfacing and impactor populations. *Science*, *329*(5998), 1504–1507. https://doi.org/10.1126/science.1195050

Kadish, S. J., Fassett, C. I., Head, J. W., D. E. Smith, M. T. Zuber, G. A. Neumann, & E. Mazarico. (2011). A global catalog of large lunar crater (≥20 km) from the Lunar Orbiter Laser Altimeter. Presented at the 42nd Lunar Planetary Science Conference, The Woodlands, TX, United States.

Kalynn, J., Johnson, C. L., Osinski, G. R., & Barnouin, O. (2013). Topographic characterization of lunar complex craters. *Geophysical Research Letters*, *40*(1), 38–42. https://doi.org/10.1029/2012GL053608

Kamata, S., Sugita, S., Abe, Y., Ishihara, Y., Harada, Y., Morota, T., et al. (2015). The relative timing of Lunar Magma Ocean solidification and the Late Heavy Bombardment inferred from highly degraded impact basin structures. *Icarus*, *250*, 492–503. https://doi.org/10.1016/j.icarus.2014.12.025

Konopliv, A. S., Park, R. S., Yuan, D.-N., Asmar, S. W., Watkins, M. M., Williams, J. G., et al. (2014). High-resolution lunar gravity fields from the GRAIL Primary and Extended Missions. *Geophysical Research Letters*, *41*(5), 1452–1458. https://doi.org/10.1002/2013GL059066

Kring, D. A. (2009). Targeting Complex Craters and Multi-Ring Basins to Determine the Tempo of Impact Bombardment While Simultaneously Probing the Lunar Interior. *Lunar Reconnaissance Orbiter Science Targeting Meeting*, *1483*, 71.

Laneuville, M., Wieczorek, M. A., Breuer, D., & Tosi, N. (2013). Asymmetric thermal evolution of the Moon. *Journal of Geophysical Research: Planets*, *118*(7), 1435–1452. https://doi.org/10.1002/jgre.20103

Laneuville, M., Taylor, J., & Wieczorek, M. A. (2018). Distribution of Radioactive Heat Sources and Thermal History of the Moon. *Journal of Geophysical Research: Planets*, *123*(12), 3144–3166. https://doi.org/10.1029/2018JE005742

Losiak, A., Wilhelms, D. E., Byrne, C. J., Thaisen, K. G., Weider, S. Z., Kohout, T., et al. (2009). A New Lunar Impact Crater Database (Vol. 40, p. 1532). Presented at the Lunar and Planetary Science Conference. Retrieved from http://adsabs.harvard.edu/abs/2009LPI....40.1532L

Milbury, C., Johnson, B. C., Melosh, H. J., Collins, G. S., Blair, D. M., Soderblom, J. M., et al. (2015). Preimpact porosity controls the gravity signature of lunar craters. *Geophysical Research Letters*, *42*. https://doi.org/10.1002/2015GL066198

Miljković, K., Collins, G. S., Wieczorek, M. A., Johnson, B. C., Soderblom, J. M., Neumann, G. A., & Zuber, M. T. (2016). Subsurface morphology and scaling of lunar impact basins. *Journal of Geophysical Research: Planets*, *121*(9), 1695–1712. https://doi.org/10.1002/2016JE005038

Miljković, Katarina, Wieczorek, M. A., Collins, G. S., Laneuville, M., Neumann, G. A., Melosh, H. J., et al. (2013). Asymmetric distribution of lunar impact basins caused by variations in target properties. *Science*, *342*(6159), 724–726. https://doi.org/10.1126/science.1243224

Nelson, D. M., Koeber, S. D., Daud, K., Robinson, M. S., Watters, T. R., Banks, M. E., & Williams, N. R. (2014). Mapping Lunar Maria Extents and Lobate Scarps Using LROC Image Products (Vol. 45, p. 2861). Presented at the Lunar and Planetary Science Conference. Retrieved from http://adsabs.harvard.edu/abs/2014LPI....45.2861N

Neukum, G., Ivanov, B. A., & Hartmann, W. K. (2001). Cratering Records in the Inner Solar System in Relation to the Lunar Reference System. *Space Science Reviews*, *96*(1), 55–86. https://doi.org/10.1023/A:1011989004263

Neumann, G. A., Zuber, M. T., Wieczorek, M. A., Head, J. W., Baker, D. M. H., Solomon, S. C., et al. (2015). Lunar impact basins revealed by Gravity Recovery and Interior Laboratory measurements. *Science Advances*, *1*(9). https://doi.org/10.1126/sciadv.1500852

Orgel, C., Michael Gregory, Fassett Caleb I., van der Bogert Carolyn H., Riedel Christian, Kneissl Thomas, & Hiesinger Harald. (2018). Ancient Bombardment of the Inner Solar System: Reinvestigation of the "Fingerprints" of Different Impactor Populations on the Lunar Surface. *Journal of Geophysical Research: Planets*, *123*(3), 748–762. https://doi.org/10.1002/2017JE005451

Pike, R. J. (1977). Size-dependence in the shape of fresh impact craters on the moon. In D. J. Roddy, R. O. Pepin, & R. B. Merrill (Eds.), *Impact and Explosion Cratering: Planetary and Terrestrial Implications* (pp. 489–509). New York: Pergamon Press.

Pilkington, M., & Grieve, R. A. F. (1992). The geophysical signature of terrestrial impact craters. *Reviews of Geophysics*, *30*(2), 161–181. https://doi.org/10.1029/92RG00192

Potter, Ross W. K., Kring, D. A., & Collins, G. S. (2013). Quantifying the attenuation of structural uplift beneath large lunar craters: ATTENUATION OF STRUCTURAL UPLIFT. *Geophysical Research Letters*, *40*(21), 5615–5620. https://doi.org/10.1002/2013GL057829

Potter, Ross W.K. (2015). Investigating the onset of multi-ring impact basin formation. *Icarus*, *261*, 91–99. https://doi.org/10.1016/j.icarus.2015.08.009

Potter, R.W.K., Collins, G. S., Kiefer, W. S., McGovern, P. J., & Kring, D. A. (2012). Constraining the size of the South Pole-Aitken basin impact. *Icarus*, *220*(2), 730–743. https://doi.org/10.1016/j.icarus.2012.05.032

Rolf, T., Zhu, M.-H., Wünnemann, K., & Werner, S. C. (2017). The role of impact bombardment history in lunar evolution. *Icarus*, *286*(Supplement C), 138–152. https://doi.org/10.1016/j.icarus.2016.10.007

Schmidt, R. M., & Housen, K. R. (1987). Some recent advances in the scaling of impact and explosion cratering. *International Journal of Impact Engineering*, *5*(1), 543–560. https://doi.org/10.1016/0734-743X(87)90069-

Smith, D.E., Zuber, M.T., Neumann, G.A., Mazarico, E., Lemoine, F.G., Head, J.W. III, Lucey, P.D., Aharonson, O., Robinson, M.S., Sun, X., Torrence, M.H., Barker, M.K., Oberst, J., Duxbury, T.C., Mao, D.-d., Barmouin, O.S., Jha, K., Rowlands, D.D. Goossens, S., Baker, D. Bauer, S., Gläser, P., Lemelin, M. Rosenburg, M., Sori, M.M., Whitten, J., McClanahan, T. (2016) Summary of the results from the Lunar Orbiter Laser Altimeter after seven years in orbit, *Icarus, 283,*70-91, doi: 10.1016/j.icarus.2016.06.006

Soderblom, J. M., Evans, A. J., Johnson, B. C., Melosh, H. J., Miljković, K., Phillips, R. J., et al. (2015). The fractured Moon: Production and saturation of porosity in the lunar highlands from impact cratering. *Geophysical Research Letters*, *42*(17). https://doi.org/10.1002/2015GL065022

Taylor, G. J., & Wieczorek, M. A. (2014). Lunar bulk chemical composition: a post-Gravity Recovery and Interior Laboratory reassessment. *Phil. Trans. R. Soc. A*, *372*(2024), 20130242. https://doi.org/10.1098/rsta.2013.0242

Tompkins, S., & Pieters, C. M. (1999). Mineralogy of the lunar crust: Results from Clementine. *Meteoritics & Planetary Science*, *34*(1), 25–41. https://doi.org/10.1111/j.1945-5100.1999.tb01729.x

Turcotte, D., & Schubert, G. (2014). *Geodynamics*. Cambridge University Press.

Whitten, J. L., & Head, J. W. (2015). Lunar cryptomaria: Physical characteristics, distribution, and implications for ancient volcanism. *Icarus*, *247*, 150–171. https://doi.org/10.1016/j.icarus.2014.09.031

Wieczorek, M. A., Neumann, G. A., Nimmo, F., Kiefer, W. S., Taylor, G. J., Melosh, H. J., et al. (2013). The crust of the Moon as seen by GRAIL. *Science*, *339*(6120), 671–675. https://doi.org/10.1126/science.1231530

Wieczorek, Mark A., & Meschede, M. (2018). SHTools: Tools for Working with Spherical Harmonics. *Geochemistry, Geophysics, Geosystems*, *19*(8), 2574–2592. https://doi.org/10.1029/2018GC007529

Wieczorek, Mark A., & Phillips, R. J. (1998). Potential anomalies on a sphere: Applications to the thickness of the lunar crust. *Journal of Geophysical Research: Planets*, *103*(E1), 1715–1724. https://doi.org/10.1029/97JE03136

Zhu, M.-H., Wünnemann, K., Potter, R. W. K., Kleine, T., & Morbidelli, A. (n.d.). Are the Moon's Nearside-Farside Asymmetries the Result of a Giant Impact? *Journal of Geophysical Research: Planets*, *0*(0). https://doi.org/10.1029/2018JE005826

Zuber, M. T., Smith, D. E., Watkins, M. M., Asmar, S. W., Konopliv, A. S., Lemoine, F. G., et al. (2013). Gravity Field of the Moon from the Gravity Recovery and Interior Laboratory (GRAIL) Mission. *Science*, *339*(6120), 668–671. https://doi.org/10.1126/science.1231507